



# A Magnetohydrodynamic Relaxation Method for Non-force-free Magnetic Field in Magnetohydrostatic Equilibrium

Takahiro Miyoshi<sup>1</sup>, Kanya Kusano<sup>2</sup> , and Satoshi Inoue<sup>2</sup>

<sup>1</sup> Graduate School of Science, Hiroshima University, 1-3-1 Kagamiyama, Higashihiroshima 739-8526, Japan; [miyoshi@sci.hiroshima-u.ac.jp](mailto:miyoshi@sci.hiroshima-u.ac.jp)

<sup>2</sup> Institute for Space-Earth Environmental Research, Nagoya University, Chikusaku Furo-Cho, Nagoya 464-8601, Japan  
 Received 2019 September 5; revised 2019 December 11; accepted 2019 December 22; published 2020 February 20

## Abstract

A nonlinear force-free field (NLFFF) extrapolation is widely used to reconstruct the three-dimensional magnetic field in the solar corona from the observed photospheric magnetic field. However, the pressure gradient and gravitational forces are ignored in the NLFFF model, even though the photospheric and chromospheric magnetic fields are not in general force-free. Here we develop a magnetohydrodynamic (MHD) relaxation method that reconstructs the solar atmospheric (chromospheric and coronal) magnetic field as a non-force-free magnetic field (NFFF) in magnetohydrostatic equilibrium where the Lorentz, pressure gradient, and gravitational forces are balanced. The system of basic equations for the MHD relaxation method is derived, and mathematical properties of the system are investigated. A robust numerical solver for the system is constructed based on the modern high-order shock capturing scheme. Two-dimensional numerical experiments that include the pressure gradient and gravitational forces are also demonstrated.

*Unified Astronomy Thesaurus concepts:* Solar magnetic fields (1503); Solar corona (1483); Solar chromosphere (1479); Solar photosphere (1518); Solar atmosphere (1477); Solar coronal loops (1485)

## 1. Introduction

Information on the three-dimensional structure of the magnetic field in the solar atmosphere (chromosphere and corona) is essential to understand and predict various solar phenomena. However, the atmospheric magnetic field has not been directly measured, whereas the vector magnetic field, i.e., all three components of the magnetic field, on the photosphere can be measured with high accuracy. Therefore, we must reconstruct the solar atmospheric magnetic field from the two-dimensional distribution of the photospheric vector magnetic field (e.g., see review by Wiegelmann & Sakurai 2012).

Since the plasma beta is low in the solar corona (Gary 2001), the pressure gradient and gravitational forces are negligible compared to the Lorentz force. Therefore, a force-free field assumption where the Lorentz force vanishes may be appropriate for the coronal magnetic field model. In particular, a nonlinear force-free magnetic field (NLFFF) model, where a factor of proportionality between the magnetic field and current density vectors is not constant, has been widely studied. Since the NLFFF cannot be analytically solved except specific configurations, various numerical methods for the NLFFF extrapolation such as the Grad–Rubin method (e.g., Sakurai 1981; Amari et al. 2006), the optimization method (e.g., Wheatland et al. 2000; Wiegelmann 2004), and the magnetofrictional or magnetohydrodynamic (MHD) relaxation method (e.g., Mikić & McClymont 1994; Valori et al. 2005; Inoue et al. 2014) have been proposed so far. All these methods well reproduce analytical force-free field models (e.g., Schrijver et al. 2006). On the other hand, the vector magnetic fields on the photosphere and in the lower chromosphere are not in general force-free (Metcalf et al. 1995) because the plasma beta below the chromosphere is order of unity or more (Gary 2001). In order to use observed non-force-free data as the boundary condition for the NLFFF model, a preprocessing procedure to minimize an integrated force over the observed region is required (Wiegelmann et al. 2006; Fuhrmann et al. 2007). The preprocessing, however, may change the

solution quantitatively or qualitatively. In fact, comparative studies using a solar-like (Metcalf et al. 2008) or observational data set (Schrijver et al. 2008; DeRosa et al. 2009) pointed out that the different NLFFF extrapolation methods with/without the preprocessing produce different magnetic field geometries and different free energies.

The preprocessing corresponds to an adjustive modeling of the photosphere-to-chromosphere as the bottom boundary of the NLFFF. In contrast, a magnetohydrostatic (MHS) equilibrium model enables us to use a non-force-free magnetic field on the photosphere directly as the boundary condition because the magnetic field in MHS equilibrium does not have to be force-free. Although general solutions for the MHS equilibrium cannot be obtained, a special class of what are called linear MHS solutions can be solved by an ansatz that the electric current consists of both a linear force-free current and horizontal non-force-free current (Low 1991). This linear MHS model was applied to a quiet-Sun region (Wiegelmann et al. 2015) and an active-Sun region (Wiegelmann et al. 2017). On the other hand, in order to solve general nonlinear MHS solutions, it is necessary to develop a more advanced numerical method. The Grad–Rubin method has been applied to solve the MHS equations without (Gilchrist & Wheatland 2013) and with the gravitational force (Gilchrist et al. 2016). The optimization method has also been extended for the system without (Wiegelmann & Neukirch 2006) and with the gravity (Zhu & Wiegelmann 2018). In these methods except the one by Zhu & Wiegelmann (2018), the pressure on the photosphere is imposed as the boundary condition. The magnetofrictional method was proposed to compute the three-dimensional equilibrium in a torus geometry including the pressure gradient force (Chodura & Schlüter 1981). Furthermore, the MHD relaxation method that solves the full compressible MHD equations has been developed (Zhu et al. 2013). The validity has been examined in comparison with an MHD simulation of an emerging flux (Zhu et al. 2013) and  $H_\alpha$  fibrils in the chromosphere (Zhu et al. 2016). The density as well as the

pressure at the bottom boundary is fixed by the values on the photosphere in this method.

In this paper, we propose a new MHD relaxation method for a non-force-free magnetic field (NFFF) in the MHS equilibrium including the pressure gradient and gravitational forces, where properly reduced compressible MHD equations are dynamically solved as a function of a virtual time  $t$ . In the previous MHD relaxation method (Zhu et al. 2013, 2016), the temperature distribution in the solar atmosphere is calculated as a result of the full compressible MHD simulation. On the other hand, in the present method, the vertical profile of temperature is given beforehand. Moreover, the previous method requires both the density and pressure values on the photosphere in addition to the vector magnetic field, while this method imposes only the vector magnetic field as the physical boundary condition. In Section 2, the MHS equilibrium problem to be solved in this method is prescribed. The basic equations and their mathematical properties are addressed in Section 3. In addition, a robust numerical scheme for the equations is presented. Simple numerical experiments are performed and discussed in Section 4. Finally, in Section 5, concluding remarks are presented.

## 2. MHS Equilibrium

Consider a dimensionless MHS equilibrium:

$$(\nabla \times \mathbf{B}) \times \mathbf{B} - \nabla p - \rho g \mathbf{e}_z = 0, \quad (1)$$

where  $\mathbf{B}$ ,  $p$ ,  $\rho$ ,  $g$ , and  $\mathbf{e}_z$  are the magnetic field, pressure, density, gravitational acceleration, and unit vector in  $z$  direction, respectively. This indicates that the Lorentz force in the MHS equilibrium does not vanish in general since it can balance both the pressure gradient and gravitational forces. We subtract a background hydrostatic field,  $p_0$  and  $\rho_0$ , from (1), and obtain

$$(\nabla \times \mathbf{B}) \times \mathbf{B} - \nabla \tilde{p} - \tilde{\rho} g \mathbf{e}_z = 0, \quad (2)$$

where

$$-\frac{\partial p_0}{\partial z} - \rho_0 g = 0. \quad (3)$$

The components deviated from the hydrostatic equilibrium are respectively

$$\tilde{p} = p - p_0(z), \quad \tilde{\rho} = \rho - \rho_0(z), \quad (4)$$

which are termed “pressure deviation” and “density deviation.” Note that these deviations are not necessarily small.

Here we assume that the temperature profile in the solar atmosphere depends only on the height  $z$  and coincides with the one determined by the background hydrostatic field as

$$T(z) = \frac{p_0(z)}{\rho_0(z)} = \frac{p}{\rho}. \quad (5)$$

Hence,

$$\tilde{\rho} = \frac{\tilde{p}}{T(z)}. \quad (6)$$

Substituting (6) into (2) yields

$$(\nabla \times \mathbf{B}) \times \mathbf{B} - \nabla \tilde{p} - \frac{\tilde{p}}{H(z)} \mathbf{e}_z = 0, \quad (7)$$

where the scale height  $H(z)$  is defined by

$$H(z) \equiv \frac{T(z)}{g}. \quad (8)$$

Consequently, the task to be addressed in this paper is to solve the MHS equilibrium field (7) with the boundary condition as

$$\mathbf{B}(x, y, z = 0) = \mathbf{B}_{\text{ph}}, \quad (9)$$

where  $\mathbf{B}_{\text{ph}}$  is the vector magnetic field on the photosphere. The background fields are not required under the assumption of (5). Meanwhile, the profile of  $H(z)$  is given beforehand in our model. This is one of the reasonable and efficient approaches because the three-dimensional temperature distribution in the solar atmosphere has not been solved consistent with the magnetic field distribution yet.

Note that Gilchrist et al. (2016) have adopted a similar approach: The density and pressure are decomposed into the background components and their deviations, respectively. The scale height is given beforehand as a function of the position, not only of  $z$ . Their approach is more general since a different scale height can be considered in a quiet or an active region. However, it is difficult to know the exact scale height in advance because the three-dimensional distribution of the magnetic field must also be determined consistently. Therefore, in the present MHS equilibrium (7), the scale height is simply given as in (8), as a function of  $z$  using typical or average values in the active region.

## 3. MHD Relaxation Method for the NFFF

### 3.1. Basic Equations

In the relaxation method for the NFFF model, as for the NLFFF model, the induction equation for the magnetic field is numerically solved until a quasi-static state is reached. The basic equations of our method are given as follows:

$$\frac{\partial \mathbf{V}}{\partial t} = (\nabla \times \mathbf{B}) \times \mathbf{B} - \nabla \tilde{p} - \frac{\tilde{p}}{H(z)} \mathbf{e}_z - \nu \mathbf{V} \quad (10)$$

$$\frac{\partial \mathbf{B}}{\partial t} = \nabla \times (\mathbf{V} \times \mathbf{B} - \eta \nabla \times \mathbf{B}) \quad (11)$$

$$\frac{\partial \tilde{p}}{\partial t} = -a^2 \nabla \cdot \mathbf{V}, \quad (12)$$

where  $\mathbf{V}$ ,  $\nu$ ,  $\eta$ , and  $a$  are the fluid velocity, friction coefficient, resistivity, and a “pseudo-speed of sound,” respectively. The Equation (10) indicates that the fluid is accelerated not only by the Lorentz force, but also the pressure gradient and gravitational forces, and decelerated by the friction that increases with the velocity. The magnetic field is evolved in time according to the induction Equation (11) including the motion-induced and resistive electric fields. In addition, the time evolution of the pressure deviation is taken into consideration. Since a physically correct time evolution of the pressure is not necessary in our method, we propose a simple evolution equation for the pressure deviation as in (12). The pseudo-speed of sound  $a$  is not a physical value but a numerical one which should be determined by numerical experiments, and is given by an arbitrary constant in this paper. Here we insist that  $\tilde{p}$  can be negative as the absolute value of the pressure does not appear in this system of equations.

Finally, we expect that the MHS equilibrium (7) is obtained since  $V$  may approach to 0 due to the friction in (10). Note that the basic equations of our method result in the equations for the NLFFF model if  $\tilde{p}$  is set to 0.

### 3.1.1. Magnetic Field-aligned Dynamics

We consider here the magnetic field-aligned dynamics in the case that  $H(z) \rightarrow \infty$ . Since the Lorentz force vanishes along the magnetic field, (10) and (12) are combined into

$$\frac{\partial^2 \tilde{p}}{\partial t^2} + \nu \frac{\partial \tilde{p}}{\partial t} - a^2 \frac{\partial^2 \tilde{p}}{\partial x_{\parallel}^2} = 0, \quad (13)$$

or

$$\frac{\partial^2}{\partial t^2} \left( \frac{\partial V_{\parallel}}{\partial x_{\parallel}} \right) + \nu \frac{\partial}{\partial t} \left( \frac{\partial V_{\parallel}}{\partial x_{\parallel}} \right) - a^2 \frac{\partial^2}{\partial x_{\parallel}^2} \left( \frac{\partial V_{\parallel}}{\partial x_{\parallel}} \right) = 0, \quad (14)$$

where  $x_{\parallel}$  and  $V_{\parallel}$  show the coordinate and velocity along a magnetic field line. The Equation (13) or (14) is the so-called telegraph equation which consists of a wave equation and a diffusion equation. Thus, bumps of  $\tilde{p}$  or  $\partial V_{\parallel} / \partial x_{\parallel}$  propagate almost at the speed  $a$  and diffuse almost at  $a^2 / \nu$ . Consequently, in the region that the scale height is large, the pressure deviation evolves so as to be uniform along the magnetic field line.

### 3.1.2. Gravitational Stability

A thermal-fluid system, in general, can be unstable to thermal convection if the gravitational effect is taken into consideration. In order for the solution of the system from (10) to (12) to converge to the static state, the system must be gravitationally stable.

We consider here the case that  $\mathbf{B} = 0$ . In this case, the system becomes linear. If periodicity in all directions and a constant  $H$  are assumed for simplicity, we obtain the following dispersion relation:

$$(\omega + i\nu)^2 \left( \omega^2 + i\nu\omega - a^2 k^2 + i \frac{a^2 k_z}{H} \right) = 0, \quad (15)$$

where  $\omega$  and  $k$  denote the frequency and wavenumber. This leads to a sufficient condition for the stability as

$$\nu > \frac{a}{H}. \quad (16)$$

See Appendix A for details. Since a line-tied magnetic field is expected to further stabilize the system, the condition (16) is sufficient to stabilize the system with the boundary condition (9).

### 3.2. Numerical Methods

A numerical solver for the system from (10) to (12) may be constructed such that the second and third terms of the right-hand side of (10) and the Equation (12) are simply discretized and added to an existing well-optimized code for the NLFFF. Here, however, we propose numerical methods that are suitable for our entire system.

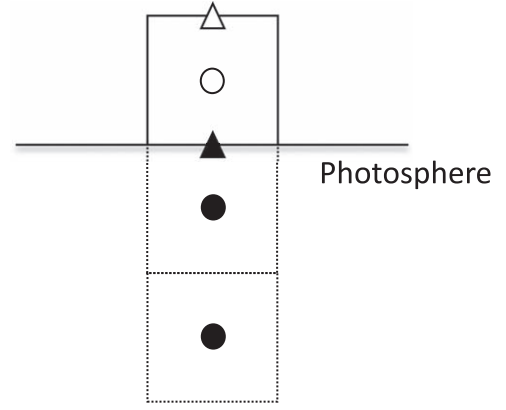


**Figure 1.** Schematic diagram of the grid structure around the photospheric boundary. The open circle shows the representative point of a cell just inside the boundary (termed as  $I$ ), whereas the filled circles are the points of ghost cells (termed as  $G$ ). The time evolution of the conservative variables in the cell  $I$  is determined by the numerical fluxes at the open and filled triangles. The variables or fluxes at the filled marks cannot be treated in the same manner as those inside the domain.

We rewrite the basic Equations (10) to (12) in the conservative form as

$$\frac{\partial \mathbf{U}}{\partial t} + \nabla \cdot \mathbf{F} = \mathbf{S}, \quad (17)$$

$$\mathbf{U} = \begin{bmatrix} \mathbf{V} \\ \mathbf{B} \\ \tilde{p} \\ \psi \end{bmatrix}, \quad \mathbf{F} = \begin{bmatrix} \left( \tilde{p} + \frac{B^2}{2} \right) \mathbf{I} - \mathbf{B}\mathbf{B} \\ \mathbf{V}\mathbf{B} - \mathbf{B}\mathbf{V} + \psi \mathbf{I} \\ a^2 \mathbf{V} \\ c_h^2 \mathbf{B} \end{bmatrix}, \quad (18)$$

where  $\mathbf{I}$  is the unit tensor, and

$$\mathbf{S} = \begin{bmatrix} -\nu \mathbf{V} \\ -\nabla \times (\eta \nabla \times \mathbf{B}) \\ 0 \\ -\frac{c_p^2}{c_h^2} \psi \end{bmatrix}. \quad (19)$$

Here we introduce an additional scalar field  $\psi$  proposed by Dedner et al. (2002) in order to maintain the divergence-free condition for the magnetic field. The temporal evolution of  $\psi$  and  $\nabla \cdot \mathbf{B}$  obeys the telegraph equation, where propagation and diffusion speeds are controlled by constants  $c_h$  and  $c_p$ . Thus,  $\nabla \cdot \mathbf{B}$  is kept as small as possible.

We solve the system of conservation laws (17) using the finite volume approach. Although simple centered-finite differences may be applicable, a tuned-artificial viscosity must be required for the numerical stability particularly in using complicated real data. Therefore, since the system is hyperbolic (see Appendix B), we construct an upwind-type scheme in which an appropriate numerical viscosity is automatically added. The numerical fluxes for (17) are evaluated as in Appendix C. Moreover, in order to achieve high-order accuracy, third-order MUSCL (Koren 1993) and third-order SSP Runge–Kutta methods (Gottlieb et al. 2001) are applied. Note that the present solver which is robust can be applied to the NLFFF reconstruction.

We must define the numerical fluxes at the domain boundary because the boundary lies on a surface of a control volume, i.e., a cell face, in our approach as shown in Figure 1. Since the

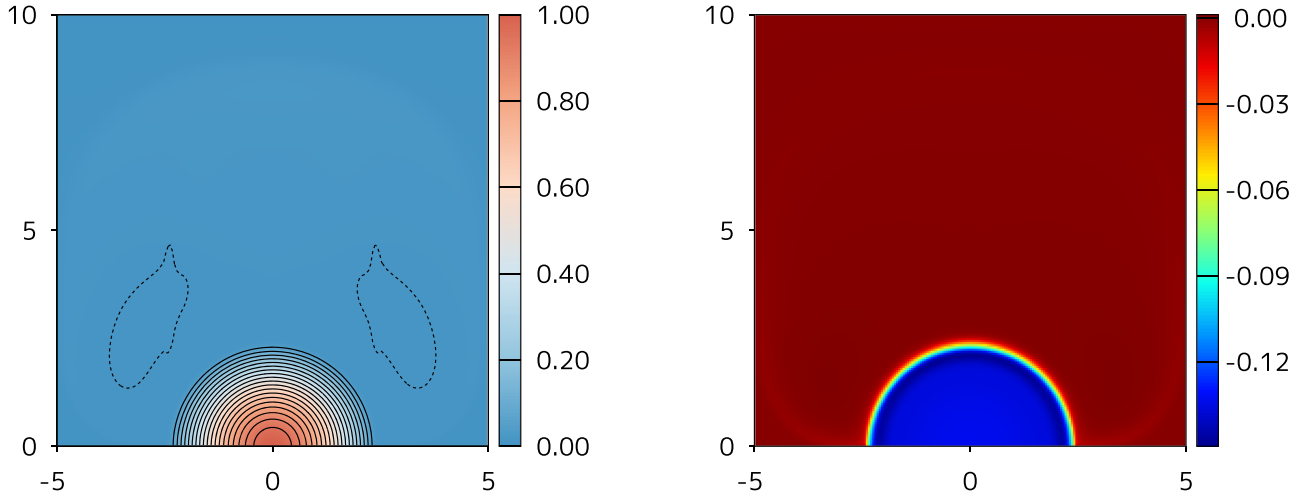


**Figure 2.** Distribution of the magnetic field and the pressure deviation for  $H(z) \rightarrow \infty$ . (Left) The lines represent contour lines for the magnetic flux-like function  $\Psi(x, z) = -\int_0^x B_z(x', 0)dx' + \int_0^z B_x(x, z')dz'$ . When the divergence-free condition of the magnetic field is satisfied,  $\Psi$  completely corresponds to the magnetic flux function. Thus, the solid and dashed lines indicate the magnetic field lines connected to and detached from the bottom boundary, respectively. The color indicates the out-of-plane magnetic field,  $B_y$ . (Right) The color indicates the pressure deviation.

vector magnetic field on the photosphere is given, all three components of the magnetic field in the numerical fluxes at the boundary as  $\mathbf{B}_h$  in (50) are fixed by (9). Moreover, two layers of ghost cells, i.e., the filled circles in Figure 1, are added outside the domain in order to compute the other variables for evaluating the numerical fluxes at the boundary, i.e., the filled triangle in Figure 1. The magnetic field in the ghost cells,  $\mathbf{B}_G$ , below the photosphere is fixed as a function of  $x$  and  $y$  as in (9). On the other hand, the pressure deviation in the photosphere cannot be measured with the same degree of accuracy as the magnetic field. Therefore, the pressure deviation in the ghost cells,  $\tilde{p}_G$ , should be given numerically, not observationally. One approach is that the pressure deviation is determined from the horizontal force balance in the ghost cells as adopted by Zhu & Wiegmann (2018). Another approach is that  $\tilde{p}_G$  is extrapolated from the physical values in the domain. Here we propose approximate outgoing characteristics at the bottom boundary,

$$dw = d\tilde{p}_T - dV_z \sqrt{a^2 + B^2}, \quad (20)$$

where  $\tilde{p}_T = \tilde{p} + B^2/2$ . If we set  $\mathbf{B} = \mathbf{B}_{ph}$ ,  $V_{zG} = 0$ , and assume  $w_G = w_I$ , where the subscript  $I$  is the index corresponding to the cell just inside the boundary, we obtain

$$\tilde{p}_G = \tilde{p}_I - V_{zI} \sqrt{a^2 + B_{ph}^2}. \quad (21)$$

Note that positive (negative)  $V_{zI}$  leads to a decrease (increase) in the pressure deviation. The top and lateral boundaries should be positioned far enough away from an active region in general. Then, for example, we assume a conducting wall, or apply some extrapolation techniques. The boundary conditions adopted in this paper are summarized in Appendix D. Although other extrapolation techniques are worth investigating, those should be examined using real data and are beyond the scope of the present study.

#### 4. Numerical Experiments

We demonstrate two-dimensional numerical experiments to investigate not only numerical stability but also the dependence of  $H(z)$  which controls the gravitational effect, in particular.

The vector magnetic field on the photosphere,  $\mathbf{B}(x, z = 0)$ , is given by

$$\begin{cases} B_x = 0, B_y = J_0(x), B_z = J_1(x) & \text{for } |x| \leq r_b \\ B_x = B_y = B_z = 0 & \text{otherwise} \end{cases} \quad (22)$$

unless otherwise stated, where  $J_\alpha$  are  $\alpha$ -th order Bessel functions of the first kind and  $r_b$  is the first zero-point of  $J_0$ , i.e.,  $J_0(r_b) = 0$ . The test problems are not so easy from the numerical stability point of view because  $B_z$  on the photosphere is discontinuous at  $r_b$ . The pressure deviation at the boundary is calculated by (21). The initial magnetic field is given by the potential field which satisfies the boundary condition of  $B_z$ . The other initial conditions are set to zero as  $|\mathbf{V}| = \tilde{p} = \psi = 0$ . The dimensions of the computational domain are  $-5 \leq x \leq 5$  and  $0 \leq z \leq 10$  in the  $x$ - and  $z$ -directions, respectively. The grid numbers are  $N_x = 200$  and  $N_z = 200$  in each direction. Number of iterations is fixed to 500,000 in all tests. The parameters to control the time evolution of the system are given by specific values as  $a = 0.4$  and  $\nu = a/H(0)$  except the case  $H \rightarrow \infty$  in this paper. The resistivity  $\eta$  is set to 0.

##### 4.1. Case $H(z) \rightarrow \infty$

First, we take notice only of the pressure gradient force. The gravitational effect in (10) is eliminated if  $H(z)$  becomes infinite. The friction coefficient  $\nu$  in this case is given by  $0.1a$ .

One of the exact solutions is that a semicylindrical force-free magnetic field,  $(B_r, B_y, B_\theta) = (0, J_0(r), J_1(r))$ , is confined by the surrounding pressure. Figure 2 shows the distribution of the magnetic field and the pressure deviation reconstructed by the present method without the gravity. The initial potential magnetic field spontaneously develops into a semicylindrical magnetic field in which the pressure deviation is almost



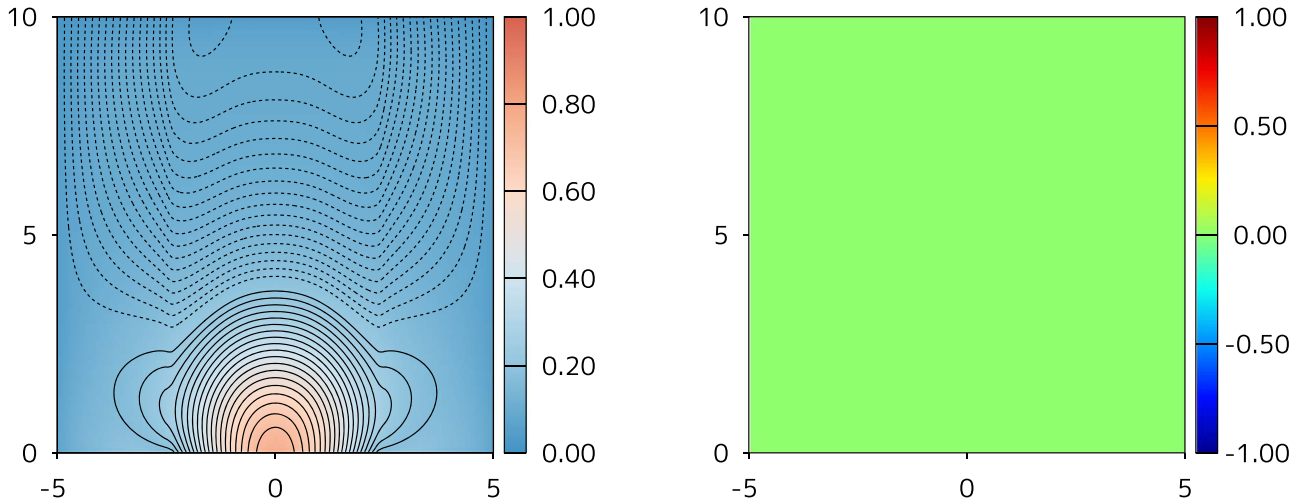


Figure 3. Same as Figure 2, but for the NLFFF.

constant. The semicylindrical configuration itself is supported by the external pressure. Note here that the pressure deviation becomes negative inside the magnetic loop since the pressure gradient force is not dependent on the absolute value of the pressure. Thus, a Bessel function-like configuration is well reproduced.

The present method results in the relaxation method for the NLFFF model if forcing the pressure deviation to zero. Thus, the NLFFF model is also computed for comparison. The distribution of the magnetic field is shown in Figure 3. The lower magnetic loop expands due to force imbalance at the bottom boundary, while the upper loop seems to be suppressed by a detached magnetic field. Here we notice that the detached magnetic field lines seem to penetrate the upper boundary incorrectly. It suggests that the NLFFF model with the NFFF boundary condition (22) does not satisfy the divergence-free condition with high accuracy.

Figure 4 shows the residual force, i.e., the first and second terms of the right-hand side of (10), as a function of iteration number. Both the mean and maximum values of the residual force for the NLFFF model are larger than one order of magnitude compared with those for the NFFF model. The increase in the residual force for the NLFFF model is expected to be due to the significant violation of the divergence-free condition near the bottom boundary.

We also perform the test without the out-of-plane magnetic field  $B_y$  at the bottom boundary instead of  $B_y = J_0(x)$  in (22). Since even the magnetic field at the boundary is completely not force-free in this case, an equilibrium distribution far away from force-free is expected. Figure 5 reveals that a semicircular magnetic field distribution similar to the poloidal field distribution in Figure 2 is reconstructed, while the pressure deviation is automatically developed so as to balance the inward Lorentz force instead of the magnetic pressure due to  $B_y$ . Conversely, the solution of the NLFFF model does not converge in this situation.

#### 4.2. Case $H(z) = \text{Const.}$

When  $H(z)$  is a sufficiently large constant as 100, a semicylindrical magnetic field distribution quite similar to that in Figure 2 is obtained. However, if  $H(z)$  becomes almost the same or smaller in size as an active region, the gravitational effect should be clearly seen. Figure 6 shows the results for the

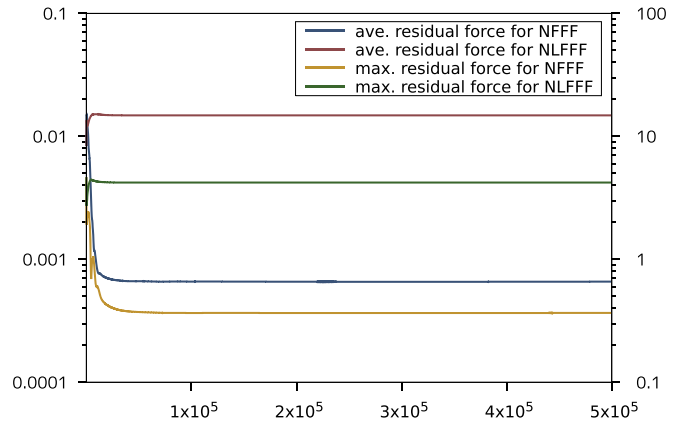


Figure 4. Residual force as a function of iteration number. The left vertical axis represents the mean of the residual force, and the right vertical axis represents the maximum value of the residual force. The bluish, reddish, yellowish, and greenish lines correspond to the mean for the NFFF, for the NLFFF, the maximum value for the NFFF, and for the NLFFF, respectively.

case  $H(z) = 3$ . The gravitational stratification leads to the pressure deviation decreasing as the height increases. Accordingly, the magnetic loop is elongated upward because the pressure gradient force that suppresses expansion of the outer magnetic loop becomes weak. Since the magnetic pressure greatly exceeds the pressure deviation at above the scale height, the reconstructed magnetic field gradually approaches the force-free field. Such a configuration will never be realized in the NLFFF model.

#### 4.3. Case $H(z) \neq \text{Const.}$

Here we adopt the following scale height profile:

$$H(z) = H_{\text{ph}} + \frac{1}{2}(H_{\text{co}} - H_{\text{ph}}) \left[ 1 + \tanh\left(\frac{z - Z_{\text{ch}}}{w}\right) \right], \quad (23)$$

where  $H_{\text{ph}}$ ,  $H_{\text{co}}$ ,  $Z_{\text{ch}}$ , and  $w$  correspond to the scale height on the photosphere, that in the corona, the thickness of the chromosphere, and the width of the transition layer from the chromosphere to the corona, respectively. The parameters are fixed as  $H_{\text{ph}} = 3$ ,  $H_{\text{co}} = 100$ , and  $w = 0.2$ .

Figure 7 shows the results for (23) with  $Z_{\text{ch}} = 1$ . The magnetic field distribution apparently resembles that for

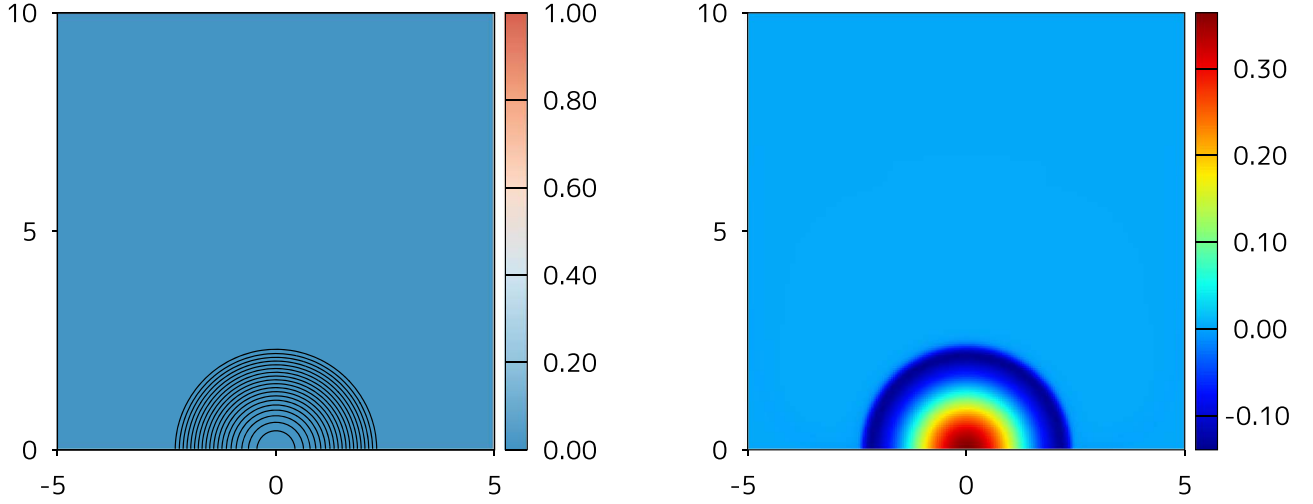


Figure 5. Same as Figure 2, but for  $B_y = 0$  at the bottom boundary.

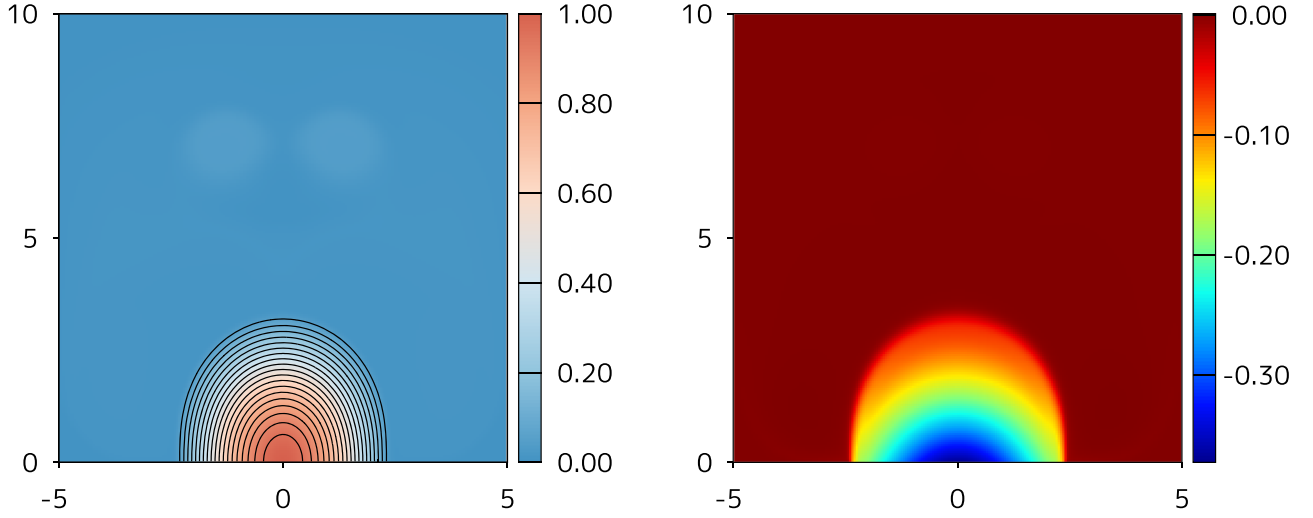


Figure 6. Same as Figure 2, but for  $H(z) = 3$ .

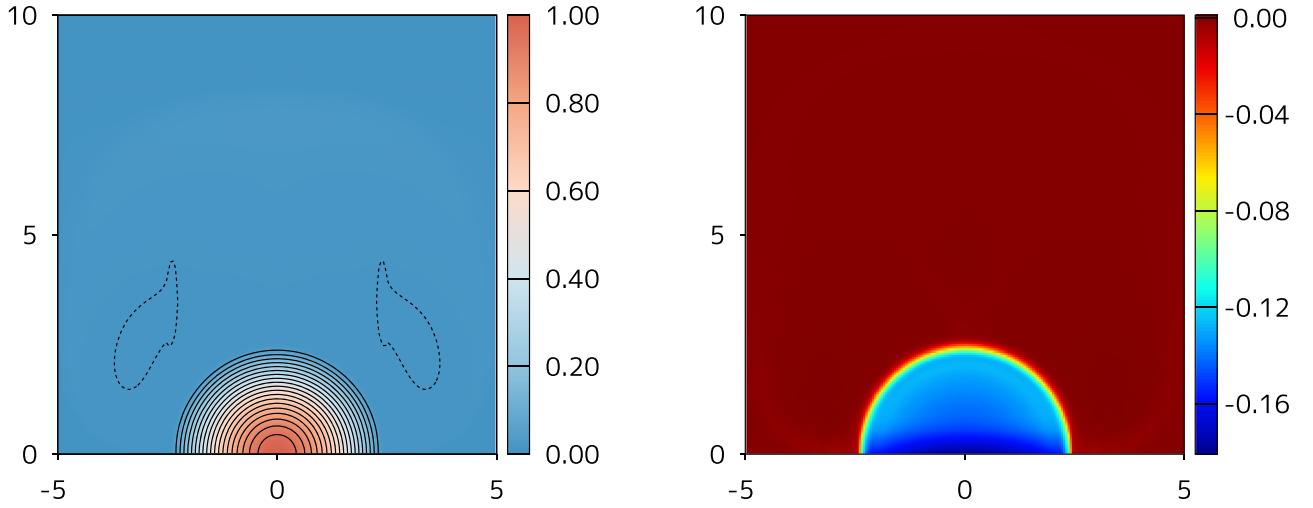


Figure 7. Same as Figure 2, but  $H(z)$  is defined by (23) with  $Z_{\text{ch}} = 1$ .

Figure 2. The pressure deviation decreases as the height increases by  $z \approx 1$ , whereas the pressure deviation at  $z > 1$ , i.e., the corona in this model, does not decrease significantly because  $H(z)$  becomes large as 100. Therefore, the coronal

magnetic field does not converge to the force-free field since the magnetic field in the lower corona is not force-free. On the other hand, when  $Z_{\text{ch}} = 4$ , which is larger than the scale height in the chromosphere, the pressure deviation decreases

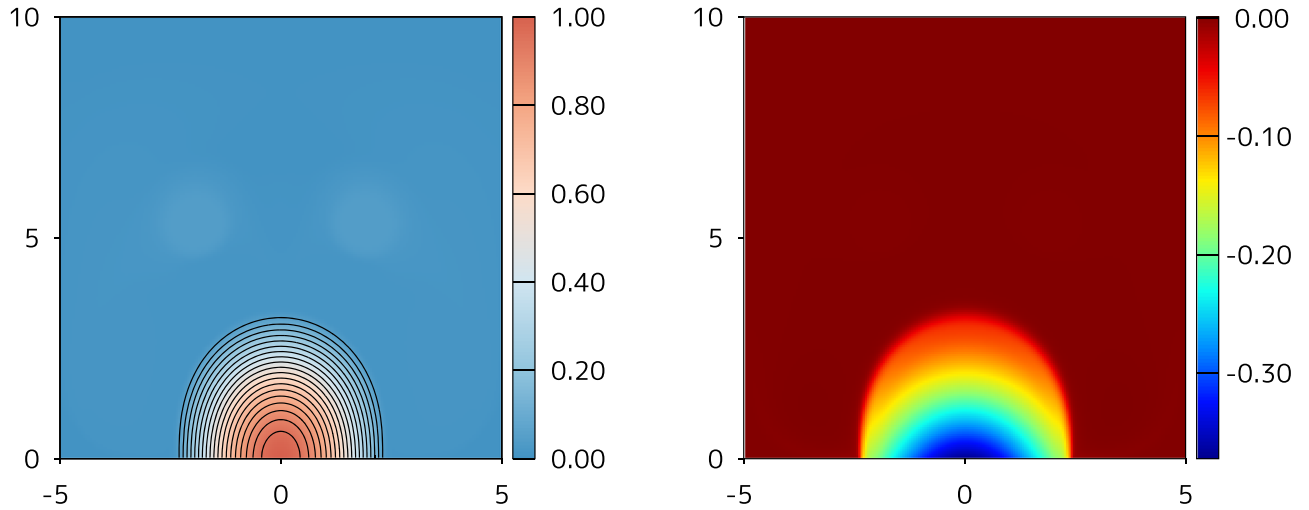


Figure 8. Same as Figure 2, but  $H(z)$  is defined by (23) with  $Z_{\text{ch}} = 4$ .

sufficiently in the chromosphere as in Figure 8. Thus, the distribution of the magnetic field as well as the pressure deviation are similar to Figure 6.

The results of the present preliminary tests suggest that small-scale magnetic fields are strongly affected by the plasma pressure and/or the gravity.

### 5. Summary

A new MHD relaxation method for the NFFF where the Lorentz force balances the pressure gradient and gravitational forces has been proposed in this paper. In particular, assuming that a temperature profile in the solar atmosphere is given beforehand and depends only on the height  $z$ , the MHD equilibrium problem is reduced to solving the magnetic field and pressure deviation for a given scale height  $H(z)$ . Therefore, the basic Equations (10) to (12) are proposed, where the pseudo-speed of sound that is not physical but numerical is employed in the evolution equation for the pressure deviation. Note here that the pressure deviation can be negative although the pressure should remain positive. The background pressure, which is determined independently of our model, must be given so that the total plasma pressure is positive. In the region of large  $H(z)$ , the pressure deviation tends to be uniform along the magnetic field according to the telegraph equation. A sufficient condition for gravitational stability of the system is also derived.

The basic equations are solved imposing only the vector magnetic field on the photosphere, where a robust high-resolution shock capturing scheme can be applied. In order to confirm the effectiveness of our method and show the difference from the NLFFF extrapolation, we particularly performed two-dimensional numerical experiments. The magnetic flux loops were able to be confined with a finite area due to the pressure gradient force in the NFFF model though those expanded to the whole domain in the NLFFF model. Some demonstrations including the gravitational effect were also carried out in this paper.

The critical assumption of the present model is that the temperature distribution is given as a function only of  $z$ . The realistic temperature distribution in the solar atmosphere, however, is not plane parallel but more complicated. When applying the present method to real data, it is necessary to

utilize a typical or an average vertical temperature profile in the active region. Moreover, since real data is dynamic and not completely MHS equilibrium, some sort of preprocessing for the photospheric vector magnetic field as in the NLFFF model (Wiegelmann et al. 2006; Fuhrmann et al. 2007) may be needed. Thus, hereafter, we need further experiments that three-dimensional magnetic fields are reconstructed using the linear MHS model (Low 1991; Zhu & Wiegelmann 2018) or observational data set, in which the temperature must be a three-dimensional distribution. A comparative study with a time-dependent MHD simulation is also worthwhile. We investigate, through the experiments, the applicability and extension of the present method whose temperature depends only on  $z$ . These are currently being studied and will be reported in our future papers.

This work was supported by MEXT/JSPS KAKENHI grant Nos. JP15K04756 (T.M.), 15H05812 and JP15H05814 (K.K.).

### Appendix A Stability Condition

Consider here a nonmagnetic system, i.e., a pure hydrodynamic system. We assume periodic boundaries in all directions and a constant scale height  $H$  for simplicity. Since the system becomes linear for the nonmagnetic system, the time evolution of Fourier modes as

$$\begin{bmatrix} \hat{V} \\ \hat{p} \end{bmatrix} \exp(-i\omega t + i\mathbf{k} \cdot \mathbf{r}), \quad (24)$$

where  $\mathbf{k}$  is the wave vector and  $\omega$  is the complex frequency, can be exactly solved. Substituting (24) into (10) with  $\mathbf{B} = 0$  and (12), we obtain the following homogeneous linear system:

$$\begin{bmatrix} \omega + i\nu & 0 & 0 & -k_x \\ 0 & \omega + i\nu & 0 & -k_y \\ 0 & 0 & \omega + i\nu & -k_z + i/H \\ -a^2 k_x & -a^2 k_y & -a^2 k_z & \omega \end{bmatrix} \begin{bmatrix} \hat{V}_x \\ \hat{V}_y \\ \hat{V}_z \\ \hat{p} \end{bmatrix} = 0. \quad (25)$$

This system has nontrivial solutions if the determinant of the coefficient matrix is zero. Thus, we obtain the dispersion

relation (15) and rewrite it as

$$(\omega + i\nu)^2 \left( \omega^2 + i\nu\omega - a^2k^2 + i\frac{a^2k_z}{H} \right) = 0. \quad (26)$$

The solutions of (26) are

$$\omega = -i\nu, \quad (27)$$

and

$$\omega = -i\frac{\nu}{2} \pm \sqrt{\xi}, \quad (28)$$

where

$$\xi = a^2k^2 - \frac{\nu^2}{4} - i\frac{a^2k_z}{H}. \quad (29)$$

The stability of the system is determined by the imaginary part of  $\omega$ . The amplitudes of the Fourier modes (24) exponentially grow in time if  $\text{Im}(\omega) > 0$ , while those exponentially decay in time if  $\text{Im}(\omega) < 0$ . Since  $\text{Im}(\omega)$  of (27) is always negative for  $\nu > 0$ , the modes are stable. On the other hand,  $\text{Im}(\omega)$  of (28) as

$$\text{Im}(\omega) = -\frac{\nu}{2} \pm \sqrt{\frac{|\xi| - \text{Re}(\xi)}{2}} \quad (30)$$

are always negative when the condition

$$\frac{\nu^2}{2} > |\xi| - \text{Re}(\xi) \quad (31)$$

is satisfied. The stability condition (31) leads to

$$\nu > \frac{a}{H} \frac{|k_z|}{|k|} \quad (32)$$

after some manipulations. Thus, the sufficient condition for the stability of the system is given by

$$\nu > \frac{a}{H} \quad (33)$$

for any wave vectors. The system is expected to be more stable when wall boundaries are considered.

### Appendix B Eigenvalues

Consider the one-dimensional system of the Equation (17) without the source terms as

$$\frac{\partial}{\partial t} \begin{bmatrix} V_x \\ V_y \\ V_z \\ B_y \\ B_z \\ \tilde{p} \end{bmatrix} + \frac{\partial}{\partial x} \begin{bmatrix} \tilde{p} + \frac{B_y^2}{2} + \frac{B_z^2}{2} - \frac{B_x^2}{2} \\ -B_x B_y \\ -B_x B_z \\ V_x B_y - B_x V_y \\ V_x B_z - B_x V_z \\ a^2 V_x \end{bmatrix} = 0, \quad (34)$$

where  $B_x$  is constant due to the divergence-free condition for the magnetic field. The Jacobian  $A$  of (34) is given by

$$A = \begin{bmatrix} 0 & 0 & 0 & B_y & B_z & 1 \\ 0 & 0 & 0 & -B_x & 0 & 0 \\ 0 & 0 & 0 & 0 & -B_x & 0 \\ B_y & -B_x & 0 & V_x & 0 & 0 \\ B_z & 0 & -B_x & 0 & V_x & 0 \\ a^2 & 0 & 0 & 0 & 0 & 0 \end{bmatrix}. \quad (35)$$

The eigenvalues  $\lambda$  of  $A$  satisfy the following characteristic equation:

$$\{\lambda(\lambda - V_x) - B_x^2\} \{\lambda^4 - V_x \lambda^3 - (B^2 + a^2)\lambda^2 + V_x a^2 \lambda + B_x^2 a^2\} = 0. \quad (36)$$

where  $B^2 = B_x^2 + B_y^2 + B_z^2$ . Two of the roots of (36) are

$$\lambda = \frac{V_x \pm \sqrt{V_x^2 + 4B_x^2}}{2}. \quad (37)$$

These correspond to the Alfvén waves. The other four roots are obtained from

$$\lambda^4 - V_x \lambda^3 - (B^2 + a^2)\lambda^2 + V_x a^2 \lambda + B_x^2 a^2 = 0. \quad (38)$$

If  $V_x = 0$ , then (38) gives

$$\lambda = \pm \sqrt{\frac{B^2 + a^2 \pm \sqrt{(B^2 + a^2)^2 - 4B_x^4 a^4}}{2}}. \quad (39)$$

Moreover, if  $B_y = B_z = 0$ ,

$$\lambda = \frac{V_x \pm \sqrt{V_x^2 + 4B_x^2}}{2}, \quad \lambda = \pm a. \quad (40)$$

Therefore, the roots of (38) indicate the magnetosonic waves. Since the eigenvalues are real, the system (34) is hyperbolic.

### Appendix C Upwind-type Scheme

Consider first the one-dimensional system of (34) as in Appendix B. Since the system is hyperbolic, an upwind-type numerical scheme enables us to realize robust computation. However, construction of Godunov's scheme or Roe's scheme for the system is neither so easy nor necessary. Therefore, a simple numerical scheme is developed here, where numerical fluxes at a cell interface are evaluated using approximate systems of equations instead of (34). We split the system of (34) into compressible ( $\partial V_x / \partial x \neq 0$ ) and incompressible ( $\partial V_x / \partial x = 0$ ) systems as follows: The compressible system is given by

$$\frac{\partial}{\partial t} \begin{bmatrix} V_x \\ \tilde{p}_{T\perp} \end{bmatrix} + \begin{bmatrix} 0 & 1 \\ a^2 + B_\perp^2 & 0 \end{bmatrix} \frac{\partial}{\partial x} \begin{bmatrix} V_x \\ \tilde{p}_{T\perp} \end{bmatrix} = 0, \quad (41)$$

where  $B_\perp^2 = B_y^2 + B_z^2$  and  $\tilde{p}_{T\perp} = \tilde{p} + B_\perp^2/2$ . The incompressible systems are given by

$$\frac{\partial}{\partial t} \begin{bmatrix} V_y \\ B_y \end{bmatrix} + \begin{bmatrix} 0 & -B_x \\ -B_x & V_x \end{bmatrix} \frac{\partial}{\partial x} \begin{bmatrix} V_y \\ B_y \end{bmatrix} = 0, \quad (42)$$

$$\frac{\partial}{\partial t} \begin{bmatrix} V_z \\ B_z \end{bmatrix} + \begin{bmatrix} 0 & -B_x \\ -B_x & V_x \end{bmatrix} \frac{\partial}{\partial x} \begin{bmatrix} V_z \\ B_z \end{bmatrix} = 0, \quad (43)$$



respectively. Thus, the magnetosonic waves and the planar Alfvén waves are decoupled. We readily derive the upwind-biased values at the cell interface, denoted by  $h$ , from (41) as

$$V_x^h = \frac{V_x^R + V_x^L}{2} - \frac{1}{2\sqrt{a^2 + B_\perp^2}}(\tilde{p}_{T\perp}^R - \tilde{p}_{T\perp}^L), \quad (44)$$

$$\tilde{p}_{T\perp}^h = \frac{\tilde{p}_{T\perp}^R + \tilde{p}_{T\perp}^L}{2} - \frac{\sqrt{a^2 + B_\perp^2}}{2}(V_x^R - V_x^L), \quad (45)$$

where the superscripts  $R$  and  $L$  indicate the right and left states at the interface. Here  $B_\perp^2$  is given by  $\max(B_\perp^{R2}, B_\perp^{L2})$  because  $B_\perp$  is not determined self-consistently. From (42),

$$V_y^h = \frac{V_y^R + V_y^L}{2} + \frac{V_x}{2\sqrt{V_x^2 + 4B_x^2}}(V_y^R - V_y^L) + \frac{B_x}{\sqrt{V_x^2 + 4B_x^2}}(B_y^R - B_y^L), \quad (46)$$

$$B_y^h = \frac{B_y^R + B_y^L}{2} + \frac{B_x}{\sqrt{V_x^2 + 4B_x^2}}(V_y^R - V_y^L) - \frac{V_x}{2\sqrt{V_x^2 + 4B_x^2}}(B_y^R - B_y^L), \quad (47)$$

and from (43),

$$V_z^h = \frac{V_z^R + V_z^L}{2} + \frac{V_x}{2\sqrt{V_x^2 + 4B_x^2}}(V_z^R - V_z^L) + \frac{B_x}{\sqrt{V_x^2 + 4B_x^2}}(B_z^R - B_z^L), \quad (48)$$

$$B_z^h = \frac{B_z^R + B_z^L}{2} + \frac{B_x}{\sqrt{V_x^2 + 4B_x^2}}(V_z^R - V_z^L) - \frac{V_x}{2\sqrt{V_x^2 + 4B_x^2}}(B_z^R - B_z^L) \quad (49)$$

are obtained using the method of characteristics. Here  $V_x$  is replaced by (44). Hence, using (44) to (49), the numerical fluxes of (34) can be evaluated as

$$F^h = \begin{bmatrix} \tilde{p}_{T\perp}^h - \frac{B_x^2}{2} \\ -B_x B_y^h \\ -B_x B_z^h \\ V_x^h B_y^h - B_x V_y^h \\ V_x^h B_z^h - B_x V_z^h \\ a^2 V_x^h \end{bmatrix}. \quad (50)$$

In order to extend to multidimensions, the divergence-free constraint of the magnetic field must be maintained numerically. Although variants of the Constrained-Transport method (e.g., Tóth 2000; Minoshima et al. 2019) where the divergence-free constraint is exactly preserved can be applied, here we adopt the hyperbolic divergence cleaning method (Dedner et al. 2002). Introduce a new scalar field  $\psi$  that corrects the magnetic field, and consider the time evolution of the numerical divergence of the magnetic field. In order to reduce the

divergence of the magnetic field  $\partial B_x / \partial x$ ,

$$\frac{\partial}{\partial t} \begin{bmatrix} B_x \\ \psi \end{bmatrix} + \begin{bmatrix} 0 & 1 \\ c_h^2 & 0 \end{bmatrix} \frac{\partial}{\partial x} \begin{bmatrix} B_x \\ \psi \end{bmatrix} = 0 \quad (51)$$

are solved in addition to (34). The upwind-biased values at the interface are evaluated as

$$B_x^h = \frac{B_x^R + B_x^L}{2} - \frac{1}{2c_h}(\psi^R - \psi^L), \quad (52)$$

$$\psi^h = \frac{\psi^R + \psi^L}{2} - \frac{c_h}{2}(B_x^R - B_x^L). \quad (53)$$

Constant  $B_x$  in the numerical fluxes of (50) is replaced by (52).

## Appendix D Boundary Conditions

At the bottom boundary that corresponds to the photosphere, the following conditions in the ghost cell are applied:

$$\begin{cases} B_G = B_{ph}, \\ V_G = 0, \\ \tilde{p}_G = \tilde{p}_I - V_{zI} \sqrt{a^2 + B_{ph}^2}, \\ \psi_G = 0, \end{cases} \quad (54)$$

where the subscripts  $G$  and  $I$  are the indices corresponding to the ghost cell and the cell just inside the boundary, respectively. The unphysical scalar field  $\psi$  correcting the magnetic field is fixed in time because of numerical stability.

At the top and lateral boundaries,

$$\begin{cases} B_G = 0, \\ V_{nG} = V_{nI} + \tilde{p}_I/a, \\ V_{tG} = 0, \\ \tilde{p}_G = 0, \\ \psi_G = \psi_I + c_h B_{nI} \end{cases} \quad (55)$$

are imposed in the numerical experiments. Here  $n$  and  $t$  indicate the normal and tangential components, in which the normal vector points outward from the domain. Assuming that  $\tilde{p}_G$  and an approximate characteristics as  $dp + dV_n a$  are zero,  $V_{nG}$  is calculated. Unlike at the bottom boundary,  $\psi_G$  is extrapolated from the inner quantities though the condition for  $\psi$  does not affect the results much.

## ORCID iDs

Kanya Kusano  <https://orcid.org/0000-0002-6814-6810>  
Satoshi Inoue  <https://orcid.org/0000-0001-5121-5122>

## References

- Amari, T., Boulmezaoud, T. Z., & Aly, J. J. 2006, *A&A*, **446**, 691
- Chodura, R., & Schlüter, A. 1981, *JCoPh*, **41**, 68
- Dedner, A., Kemm, F., Kröner, D., et al. 2002, *JCoPh*, **175**, 645
- DeRosa, M. L., Schrijver, C. J., Barnes, G., et al. 2009, *ApJ*, **696**, 1780
- Fuhrmann, M., Seehafer, N., & Valori, G. 2007, *A&A*, **476**, 349
- Gary, G. A. 2001, *SoPh*, **203**, 71
- Gilchrist, S. A., Braun, D. C., & Barnes, G. 2016, *SoPh*, **291**, 3583
- Gilchrist, S. A., & Wheatland, M. S. 2013, *SoPh*, **282**, 283
- Gottlieb, S., Shu, C. W., & Tadmor, E. 2001, *SIAMR*, **43**, 89
- Inoue, S., Magara, T., & Pandey, V. S. 2014, *ApJ*, **780**, 101
- Koren, B. 1993, in *Numerical Methods for Advection-Diffusion Problems*, ed. C. B. Vreugdenhil & B. Koren (Braunschweig: Vieweg), 117
- Low, B. C. 1991, *ApJ*, **370**, 427

- Metcalf, T. R., DeRosa, M. L., Schrijver, C. J., et al. 2008, [SoPh](#), **247**, 269
- Metcalf, T. R., Jiao, L., McClymont, A. N., Canfield, C., & Uitenbroek, H. 1995, [ApJ](#), **439**, 474
- Mikić, Z., & McClymont, A. N. 1994, in ASP Conf. Ser.68, Solar Active Region Evolution: Comparing Models with Observations, ed. K. S. Balasubramaniam & G. W. Simon (San Francisco, CA: ASP), **225**
- Minoshima, T., Miyoshi, T., & Matsumoto, Y. 2019, [ApJS](#), **242**, 14
- Sakurai, T. 1981, [SoPh](#), **69**, 343
- Schrijver, C. J., DeRosa, M. L., Metcalf, T. R., et al. 2006, [SoPh](#), **235**, 161
- Schrijver, C. J., DeRosa, M. L., Metcalf, T. R., et al. 2008, [ApJ](#), **675**, 1637
- Tóth, G. 2000, [JCoPh](#), **161**, 605
- Valori, G., Kliem, B., & Keppens, R. 2005, [A&A](#), **433**, 335
- Wheatland, M. S., Sturrock, P. A., & Roumeliotis, G. 2000, [ApJ](#), **540**, 1150
- Wiegmann, T. 2004, [SoPh](#), **219**, 87
- Wiegmann, T., Inhester, B., & Sakurai, T. 2006, [SoPh](#), **233**, 215
- Wiegmann, T., & Neukirch, T. 2006, [A&A](#), **457**, 1053
- Wiegmann, T., Neukirch, T., Nickeler, D. H., et al. 2015, [ApJ](#), **815**, 10
- Wiegmann, T., Neukirch, T., Nickeler, D. H., et al. 2017, [ApJS](#), **229**, 18
- Wiegmann, T., & Sakurai, T. 2012, [LRSP](#), **9**, 5
- Zhu, X. S., Wang, H. N., Du, Z. L., & Fan, Y. L. 2013, [ApJ](#), **768**, 119
- Zhu, X. S., Wang, H. N., Du, Z. L., & He, H. 2016, [ApJ](#), **826**, 51
- Zhu, X. S., & Wiegmann, T. 2018, [ApJ](#), **866**, 130